Neutrally stable double-curved shells by inflection point propagation

Kok, Sjaak; Nobaveh, Ali Amoozandeh; Radaelli, Giuseppe

DOI
10.1016/j.jmps.2022.105133

Publication date
2023

Document Version
Final published version

Published in
Journal of the Mechanics and Physics of Solids

J. Mech. Phys. Solids 171 (2023) 105133

Contents lists available at ScienceDirect

Journal of the Mechanics and Physics of Solids

journal homepage: www.elsevier.com/locate/jmps

Neutrally stable double-curved shells by inflection point propagation

Sjaak Kok, Ali Amoozandeh Nobaveh, Giuseppe Radaelli *

Department of Precision and Microsystems Engineering, Delft University of Technology, Delft, 2628 CD, The Netherlands

ARTICLE INFO

Keywords:
Compliant shell mechanisms
Neutral stability
Static balance
Zero stiffness
Multi-stability
Thin-walled

ABSTRACT

Elastic structures that can deflect without springback, known as neutrally stable structures, form a remarkable group within their field, since they require the energetic state to remain unchanged during elastic deformation. Several examples in the literature obtain this state of neutral stability by the application of pre-stress, either as a result of manufacturing processes or the application of imposed boundary conditions. In this paper, we present a new class of neutrally stable structure that exhibits neutral stability as part of a continuous deformation process, while also allowing a stress-free configuration to exist. The transition of a double-curved compliant shell from its stress-free stable equilibrium towards its second stable equilibrium, through a range of neutrally stable equilibrium configurations forms the basis of this investigation. To design this neutrally stable shell, an optimization is employed to obtain an ideal set of variables that defines a varying thickness profile. Numerical analysis of the resulting optimized shell structure predicts a substantial region of near-constant energy and associated near-zero loads within this unique deformation mode. Additively manufactured prototypes demonstrate the validity of the modeled results by featuring a continuous equilibrium within the range of motion. These results lay the foundation for compliant beam elements with a neutrally stable bending degree of freedom.

1. Introduction

Compliant shell mechanisms have become an interesting research topic over recent years and have been circumstantially investigated. Relevant applications can be found in e.g. the aerospace industry, where complex requirements are expected from a slender, lightweight structure and wearable devices, where the potential arises for organically-shaped functional structures that fit closely to the human body. As a group within the increasingly popular research area of compliant mechanisms, compliant shells can be described as 'spatially curved thin-walled structures able to transfer or transmit force, motion or energy through elastic deflection' (Radaelli and Herder, 2017). A high degree of design freedom allows for the development of compliant mechanisms with non-linear force–deflection behavior, e.g. weight balancing mechanisms.

Compliant shell mechanisms that are continuously in static equilibrium throughout their range of motion belong to the group of neutrally stable structures, also known as statically balanced compliant mechanisms (SBCMs) (Herder and Van Den Berg, 2000; Gallego, 2013). As a design tool, shape optimization can be used to develop complex geometries that follow any desired load–displacement path (Radaelli and Herder, 2017; Amoozandeh Nobaveh et al., 2020, 2022). SBCMs are typically designed for weight balancing and exhibit neutral stability in presence of an external, gravitational force (Alkisaei, 2016; Radaelli and Herder, 2015, 2017). Other applications require this state of neutral stability to occur in absence of external loads (Schultz et al., 2008; Murphey

* Corresponding author.
E-mail address: g.radaelli@tudelft.nl (G. Radaelli).

https://doi.org/10.1016/j.jmps.2022.105133
Received 7 April 2022; Received in revised form 6 September 2022; Accepted 4 November 2022
Available online 17 November 2022

and Pellegrino, 2004). In the last case, the *elastic* energy in the compliant shell is required to remain constant within the range of motion. Energy is initially stored in the form of pre-stress and redistributed within the structure itself to allow deformation to occur without the need for any additional energy.

Pre-stress can be the result of an assembly process wherein multiple elastic elements are connected in such a way that no zero-energy configuration exists. Weaver and co-workers describe a moment-free pitch adjustment in airplane wings, realized by adding a pre-deformed compliant shell structure that provides negative stiffness (Lachenal et al., 2012; Daynes and Weaver, 2013; Lachenal et al., 2013; Daynes et al., 2015). Likewise, the composition of two cylindrical shells with opposite curvature senses and perpendicular directions can result in neutral stability (Murphey and Pellegrino, 2004), with applications such as deployable booms for space exploration. Shell mechanisms containing only a single element obtain their state of pre-stress via various processes, as shown in Kok (2020). For example, Guest describes a cylindrically curved compliant shell that shows neutral stability after introducing pre-stress by plastic deformation (Guest, 2011). Also, the curing process of anisotropic laminates leaves residual thermal stresses behind and can be used to generate the required pre-stress. This has been successfully implemented as a method for reducing the stiffness of compliant shells, as described by Doornenbal (2018) and Stacey et al. (2019). In nature, differential growth can result in pre-stress, causing structures to obtain their characteristic shapes (Audoly and Boudaoud, 2002; Goriely, 2017; Lessinnes et al., 2017).

The tape loop, first thoroughly investigated by Vehar et al. is an example of pre-stress resulting from boundary conditions (Vehar et al., 2004). The location of the folds, which arise when connecting the ends of a standard tape spring into a loop, is arbitrary due to its constant cross-section. The folded regions can be propagated through the structure without energetic costs, creating a neutrally stable deformation mode.

Until recently, all neutrally stable shell structures described in the literature required either the introduction of pre-stress during the manufacturing process or external constraints to be enforced continuously during neutrally stable deformation. The three methods that are used to introduce pre-stress are: combining multiple components in a pre-stressed assembly, plastically deforming material to obtain a state of self-stress and introducing residual thermal stresses during the curing process of laminates. These methods all result in a complex and sensitive manufacturing process (Kok, 2020). In addition, a structure that is pre-stressed during fabrication may suffer from deteriorating performance over time because of creep and stress relaxation (Howell et al., 2013). The required presence of boundary conditions, either in the form of external- or internal constraints, e.g. a looped geometry, limits design freedom, thereby narrowing down the potential applications. Prior work (Kok et al., 2021) resolves these issues by introducing a neutrally stable compliant shell structure that does not rely on pre-stressing during fabrication. Similar to the tape loop, it involves the propagation of a region of localized strains, though it lifts the requirement of a looped geometry, resulting in an open-ended structure. However, the structure comprises an idealized zero-stiffness crease, causing a discontinuity in the structure that complicates physical realization and obstructs its potential applications. In the case where the geometry would be constructed as a continuous shell, i.e. where the ideal crease assumption is not valid anymore, crease stiffness is introduced and therefore, the achieved neutral stability is lost. It is hypothesized that there are modifications to the shell geometry that would counteract the action of the crease, restoring the neutral stability.

In the present work the crease is replaced by a strip with negative Gaussian curvature. Giomi and Mahadevan (2012) show that this type of shape can be bi-stable and even tri-stable under certain conditions related to the shape and to the anisotropy of the material. In their theoretical treatise the deformation of the shell is driven by an uniform curvature change across the length of the strip. In present work we propose to apply a deformation that, starting with an initial reversal of the curvature at one end of the strip, gradually expands the reversed region until the whole geometry is reversed, reaching the secondary stable position also shown in Giomi and Mahadevan (2012). The aim is to generate and optimize a neutrally stable transition zone between the two stable configurations.

The goal of this research is to develop a monolithic compliant shell mechanism that features a neutrally stable deformation mode without the need for pre-stress during manufacturing or special boundary conditions to be applied. A unique and promising deformation mode of a double-curved compliant shell structure will be investigated. It features the transition between two naturally occurring stable configurations via elastic, ideally energy-conserving, deformation. Interplay occurs between the so-called ‘flange’ - and ‘crease’ sections. The influence of the geometric design parameters, e.g. crease radius and local flange thickness, on its neutrally stable potential is therefore examined.

In the next section, the shell structure with its intended deformation mode is introduced. The geometrical aspects and the mechanics of the transition are illustrated and its natural bi-stable behavior is explained by the derivation of an analytical approximation of the mechanics. In the methods section, a design approach is substantiated and the numerical modeling setup and optimization procedure are described. The design of an experimental setup and practical considerations for manufacturing prototypes are also discussed. The results section presents both the modeled and the experimental results, followed by a discussion and a conclusion.

2. Mechanics of transition

This section serves to introduce the shell structure by describing its features and design parameters and to give an intuitive understanding of its mechanical behavior. Aspects with regard to the intended deformation mode, featuring a transition region, are first elucidated and illustrated by a schematic representation of the expected energy–deflection behavior. This is further substantiated by an analytical derivation of the mechanics that predicts the same bi-stable behavior.

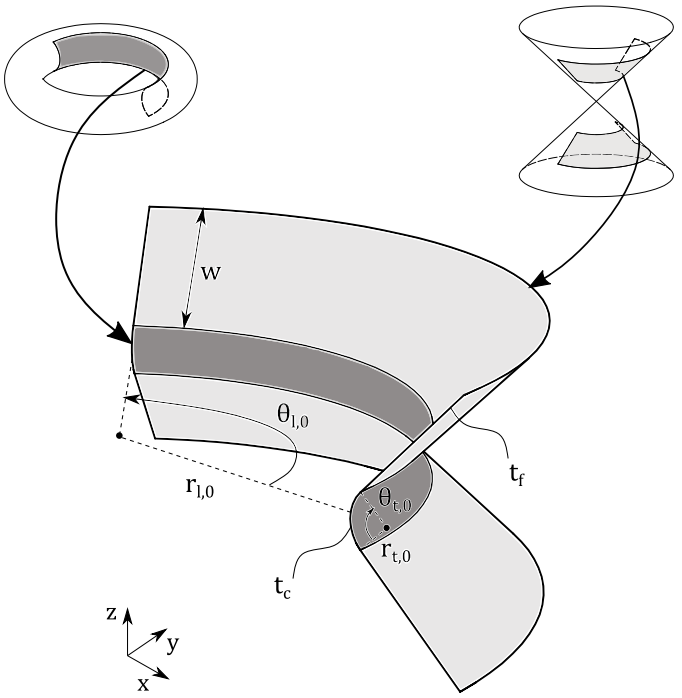

Fig. 1. The geometry of the shell structure is composed of a torus surface section with negative Gaussian curvature and two symmetric cone surface sections with zero Gaussian curvature. The design parameters that define the undeformed geometry are depicted.

2.1. Geometry description and design parameters

This investigation is based on a compliant shell structure with specific geometrical features, wherein two parts with different functionalities can be distinguished. The base of the mechanism resembles the surface section of a torus with negative Gaussian curvature, effectively forming a so-called 'curved crease'. Its two principal curvatures are perpendicular in direction and opposite in sign (Fig. 1). The two longitudinal edges are tangentially extended to create two symmetric cone surface sections, from now on referred to as the 'flanges'.

The undeformed geometry is parameterized by the width of the flanges, w, the longitudinal and transverse radius, $r_{l,0}$ and $r_{t,0}$ and the associated longitudinal- and transverse subtended angles, $\theta_{l,0}$ and $\theta_{t,0}$, that determine the overall length of the structure and the initial angle between the flanges respectively. Variables t_c and t_f denote the crease and flange thickness respectively. The radius of the circular boundary between the crease and flange sections is assumed to be equal to $r_{l,0}$ since $\frac{r_{t,0}}{r_{l,0}}$ is designed to be small.

2.2. Deformation process: initiating a transition region

A characteristic property of this group of shell structures is the existence of a second stable, though non-zero energy, configuration, from hereon referred to as the 'inverted state'. Bi-stable behavior of similar compliant shells, both with and without Gaussian curvature, is discussed in the context of laminated composites (Galletly and Guest, 2004; Knott and Viquerat, 2016, 2018, 2019). In this research, so-called 'slit tubes' form either positive- or negative barrel-shaped coils at their second equilibrium configuration when a positive- or negative longitudinal curvature is applied respectively. The shell structure that forms the basis of this research differentiates itself by its material isotropy, yet shows resemblance regarding its mechanical behavior.

A practically feasible method to obtain the second stable configuration involves the introduction and propagation of a *transition region* (Fig. 2, top). It is initiated when the flanges at one end of the structure are rotated with respect to each other around the crease until the previously opposing faces point away from each other (1). A comprehensive description of this process is given in Kok et al. (2021). The emerging transition region is characterized by high localized strains, predominantly present in the flanges. Its location s is defined as the normalized location of the inflection point along the symmetry line, or 'spine'. Its formation can be considered as the required pre-stressing part of the deformation process or, analogue to chemical reactions, as the activation energy required to initiate a sequence of events. The associated energy is referred to as the 'transition energy' and characterized by a steep energy increase with respect to variable s, as shown in Fig. 2.

As the transition region is propagated in the longitudinal direction, the structure is progressively inverted (2). With a resemblance to tape loop behavior, the geometry of the transition region and associated transition energy are roughly preserved along its way. However, an increasing part of the crease section is deformed, accounting for an approximately linear energy increase in the

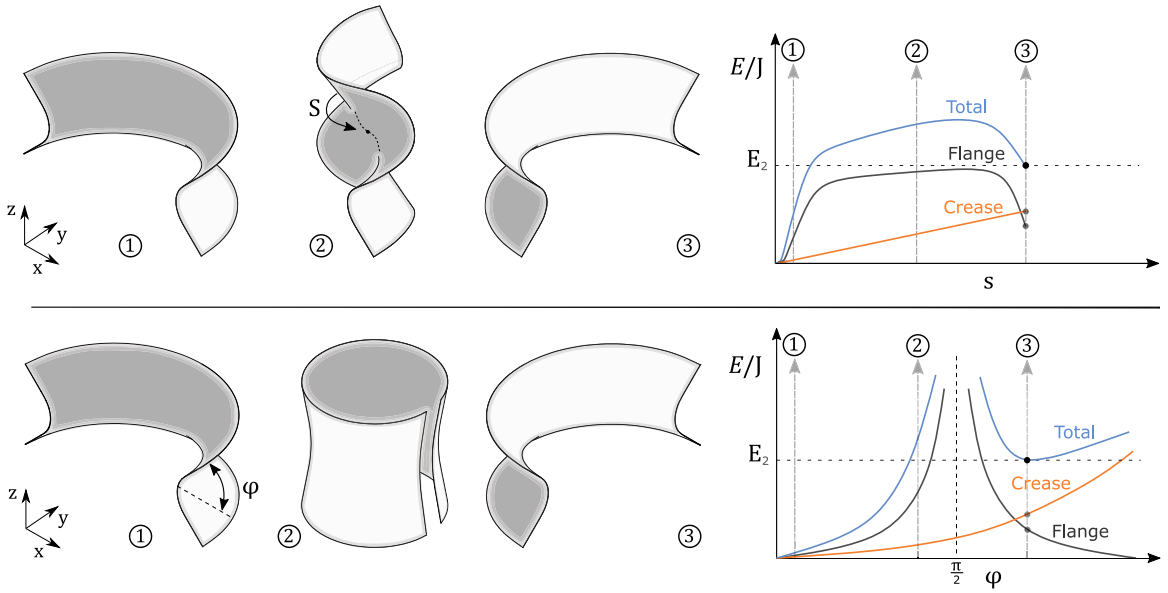

Fig. 2. The inverted state can be obtained in practice by the initiation of a transition region (top). Its location is defined as the location of the inflection point of the spine, annotated by the normalized dimensionless distance s along the spine of the shell structure. The deformation process is depicted in step (1)–(3) and a schematic energy plot gives an impression of the energetic state throughout the transition. The existence of an inverted stable equilibrium can also be shown by relating the elastic energy to the inclination angle φ of the flanges (bottom) where the energetic paths are plotted based on the analytical expressions from Eq. (15)–(17). Note that, although the deformation paths are fundamentally different, the end states (3) and associated energy levels E_2 are identical.

succeeding part of the transition. Edge effects allow the transition energy to gradually decrease to zero towards the end, leaving behind the structure in its fully inverted, non-zero energy state (3).

2.3. An analytical approach

2.3.1. Inextensibility and shell assumptions

In this section, the geometry is assumed to be inextensional, which is valid for thin shells whereby the energy required for in-plane stretching is orders of magnitude higher than for bending (Calladine, 1989). As a result of this assumption, Gaussian curvature remains invariant upon deformation and kinematic relations can be approximated. A second assumption is that circular cross-sections remain circular during the application of a load. Both these conditions enable an analytical approach to the mechanics of the shell structure. To provide a natural understanding of its mechanical properties, an alternative deformation process is described wherein the deformation is applied uniformly along the longitude of the shell (Fig. 2, bottom). This analysis predicts the same two stable equilibrium positions, yet it shows the impossibility to reach one from the other because an infinite energy configuration is encountered along its deformation path.

2.3.2. Kinematic coupling

The flanges can be considered as surface segments of a cone and are therefore developable, meaning that one of the two principal curvatures equals zero, i.e. they have zero Gaussian curvature. The toroidal section that connects the flanges can be regarded as a curved crease of circular cross-section. Because of its curved nature, actuation by varying the angle φ also results in deformation of the compliant flanges. Following the inextensibility assumptions, the kinematic relationship between the constitutive elements can be approximated.

Variation of the generalized coordinate φ results in a geometric change of both the crease and the flanges (Figs. 3(a) and 3(b)), where the following relation applies to the undeformed geometry:

$$\varphi_0 = \frac{\pi - \theta_{t,0}}{2}. \tag{1}$$

The transverse radius and associated curvature of the crease are directly linked to the angular deflection between the flanges via conservation of the arc length, according to:

$$r_t = \frac{\theta_{t,0}\, r_{t,0}}{\pi - 2\varphi} \tag{2}$$

$$\kappa_t = \frac{1}{r_t} = \frac{\pi - 2\varphi}{\theta_{t,0}\, r_{t,0}}. \tag{3}$$

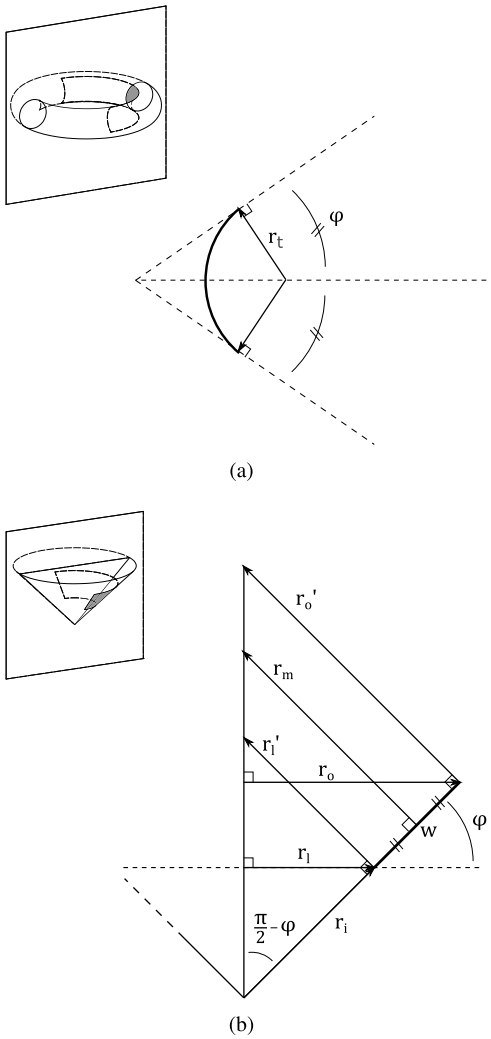

Fig. 3. A cross-section of the torus (a) and cone (b) shows the kinematic relationship between the crease and flange geometry. The flange angle φ is considered as the generalized coordinate.

Substitution of Eq. (1) in Eq. (2) results in the initial transverse radius $r_{t,0}$.

The longitudinal radius of curvature r_l follows from the inextensibility assumption and can be analytically derived by projecting the flange geometry on a cone with variable pitch (Fig. 3(b)). The kinematic relation between the flange angle φ and longitudinal radius of the crease r_l is calculated via the invariant distance r_i:

$$r_i = \frac{r_{l,0}}{\cos(\frac{\pi-\theta_{t,0}}{2})} \tag{4}$$

$$r_l = r_i \cos(\varphi), \tag{5}$$

where substitution of Eq. (1) in Eq. (5) results in the initial longitudinal radius $r_{l,0}$. The longitudinal curvature change of the crease section is omitted for simplicity, since it is designed to be small compared to κ_t.

The curvature of the cone-shaped flanges is approximated as the average of the surface curvature along the most inner- and outer perimeters with radius r_l and r_o respectively, via calculation of their local radius of *surface* curvature, according to:

$$r_l' = \frac{r_l}{\sin(\varphi)} \tag{6}$$

$$r_o' = r_l' + \frac{w}{\tan(\varphi)} \tag{7}$$

$$r_m = \frac{r_l' + r_o'}{2} \tag{8}$$

$$\kappa_{\mathrm{m}} = \frac{1}{r_{\mathrm{m}}}. \tag{9}$$

The curvature change of all elements is then given by the difference between the curvature of the undeformed and the deformed geometry, as:

$$\Delta\kappa_{\mathrm{t}} = \kappa_{\mathrm{t}}(\varphi) - \kappa_{\mathrm{t}}(\varphi_0) \tag{10}$$

$$\Delta\kappa_{\mathrm{m}} = \kappa_{\mathrm{m}}(\varphi) - \kappa_{\mathrm{m}}(\varphi_0). \tag{11}$$

2.3.3. Elastic energy relations

The energy associated with elastic deformation that follows a linear material law is given by (Calladine, 1989):

$$\mathcal{E} = \frac{1}{2}\int_A \begin{bmatrix}\boldsymbol{\gamma}\\ \boldsymbol{\Delta\kappa}\end{bmatrix}^{\mathrm{T}} \begin{bmatrix}\mathbf{A} & \mathbf{B}\\ \mathbf{B} & \mathbf{D}\end{bmatrix} \begin{bmatrix}\boldsymbol{\gamma}\\ \boldsymbol{\Delta\kappa}\end{bmatrix} dA, \tag{12}$$

where $\boldsymbol{\gamma}$ and $\boldsymbol{\Delta\kappa}$ denote the membrane stretch and curvature *change* vectors respectively that are related to the energy $\mathcal{E}$ via the ABD-matrix and surface area A. For thin shells that meet the inextensibility condition, no stretching of the mid-plane is assumed, i.e. $\boldsymbol{\gamma} = 0$. Evaluating the elastic energy per longitudinal radial unit length of shells with initial curvature, this simplifies to:

$$\frac{\mathcal{E}}{\theta_{l,0}} = \mathcal{E}' = \frac{1}{2}\int_S \boldsymbol{\Delta\kappa}^{\mathrm{T}}\mathbf{D}\boldsymbol{\Delta\kappa}\, dS, \tag{13}$$

where length unit S denotes the location in transverse direction of either the circular crease or the flanges. Matrix $\boldsymbol{D}$ contains the local material properties in accordance with (Calladine, 1989):

$$\boldsymbol{D} = \frac{Et^3}{12\left(1-\upsilon^2\right)}\begin{bmatrix}1 & \upsilon & 0\\ \upsilon & 1 & 0\\ 0 & 0 & \frac{1-\upsilon}{2}\end{bmatrix}. \tag{14}$$

When the elastic energy of the curved crease section is superimposed on the elastic energy of the flanges, the total energy follows from the sum of its individual components:

$$\mathcal{E}'_{\mathrm{c}} = \frac{1}{2}\mathbf{D}_{\mathrm{c},(1,1)}\,\Delta\kappa_{\mathrm{t}}{}^2\,\theta_{\mathrm{t},0}\,r_{\mathrm{t},0}\,r_{\mathrm{l},0} \tag{15}$$

$$\mathcal{E}'_{\mathrm{f}} = \frac{1}{2}\mathbf{D}_{\mathrm{f},(1,1)}\,\Delta\kappa_{\mathrm{m}}{}^2\,(wr_{\mathrm{l},0} + \frac{1}{2}w^2) \tag{16}$$

$$\mathcal{E}'_{\mathrm{tot}} = \mathcal{E}'_{\mathrm{c}} + 2\,\mathcal{E}'_{\mathrm{f}}, \tag{17}$$

with subscript 'c' and 'f' denoting the (material) properties of the crease and the flanges respectively. The bottom right of Fig. 2 shows a schematic plot of the energy paths, described by Eqs. (15), (16) and (17) for a geometry with initially parallel flanges (i.e. $\varphi_0 = 0$). According to Eqs. (4), (5), (7)–(10) and (16), the flange energy follows a $\tan(\varphi)^2$ trajectory and shows symmetric behavior around the asymptote $\varphi = \pi/2$. Note that, with the goal of examining the stability, an alternative deformation mode is investigated. Energy approaches infinity when $\varphi = \pi/2$, before showing a decrease in energy for values of $\varphi > \pi/2$. The transverse component of the crease energy follows a quadratic increase (Eqs. (3), (10) and (15)). Together, this predicts the theoretical existence of a second stable, though non-zero energy configuration: the inverted state. At this local energy minimum, the tendency of the flanges to flatten opposes the tendency of the crease towards its as-fabricated state, resulting in static balance. However, approaching the inverted state through this deformation process is not possible in practice since it requires a configuration with infinite strain energy.

The two discussed energetic paths required to obtain the second stable state (Fig. 2) are fundamentally different, yet their final configurations (3) are equal.

3. Methods

3.1. Conceptual approach

The energetic path obtained during propagation of the transition region is the result of a complex interplay between the various elements in the structure and is ultimately determined by the design parameters. A stiff crease, either caused by a small transverse radius or a relatively large thickness, results in a more pronounced energy increase during propagation of the transition region, as illustrated in Fig. 2. Since this effect negatively influences the neutrally stable transition, a logical approach would first of all be to minimize the crease stiffness.

Fig. 4 shows the hypothesized schematic energy profile (blue) of a standard (dashed) and a desired geometry (solid). Both cases feature a loading region that can be considered as the pre-stressing action, which is required for neutral stability to occur (Guest, 2011). In case of the standard geometry, it is followed by a significant region dominated by crease energy increase and ends with an unloading region, that leaves the structure in its inverted state. Prior research (Kok et al., 2021) has shown that the energetic contribution of the flanges (black) during propagation of the transition region is tune-able to a high extent. This gives rise to the

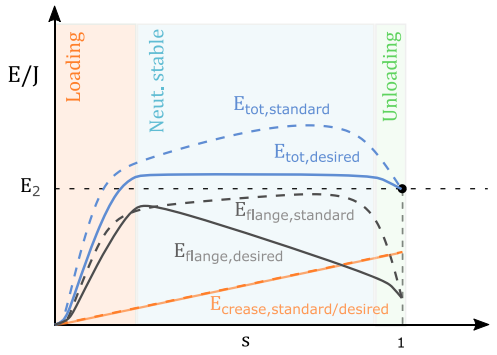

Fig. 4. A schematic representation of the hypothesized energy curves belonging to the constitutive parts during transition. The dashed and solid lines represent the standard and desired, i.e. neutrally stable, geometry respectively.

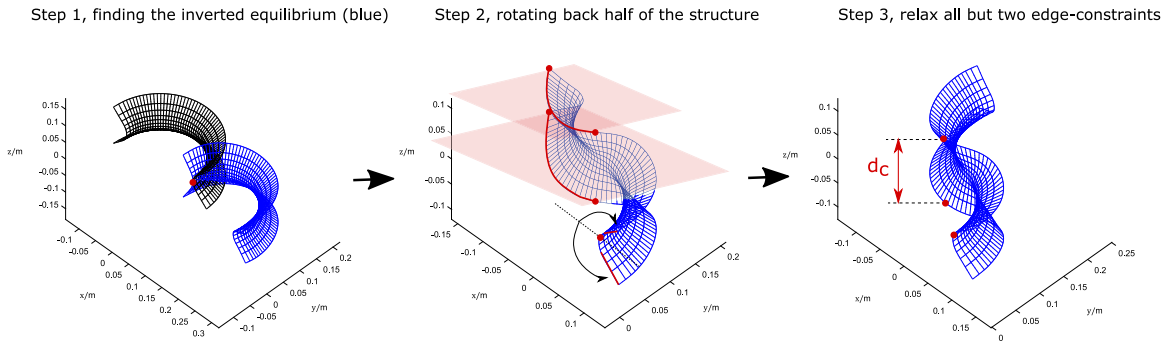

Fig. 5. The process of pre-loading the continuous shell structure involves finding the inverted equilibrium (step 1, blue), back-rotation of the flanges while constraining a significant part of the edges in height (step 2) and relaxing all but two of the edge-constraints to locally 'pinch' the structure (step 3). Note that all red colored nodes are constrained.

possibility to compensate for the increasing crease energy (orange) during transition by manipulation of the local properties of the flanges. Specifically, it requires an approximately linear decrease of the flange energy component with an equal slope of opposite sign.

Several methods have been shown to be effective for manipulating the local energy storage in the flanges (Kok et al., 2021). In this investigation, a material thickness variation in longitudinal direction is applied to the flanges, while maintaining a constant, sufficiently small, material thickness of the crease. The rationale behind this choice will be elucidated in the subsequent sections.

3.2. Numerical simulation

3.2.1. Model setup

The shell structure is modeled according to the Kirchhoff–Love plate theorem and a linear isotropic elastic constitutive law is applied to describe its elastic behavior. An isogeometric framework forms the basis of the numerical analysis, whereby the geometry is described using B-splines (Hughes et al., 2005). A Newton–Raphson numerical integration scheme is used to solve for the static equilibrium configurations.

The control points that define the B-splines are placed in the transverse (u)- and longitudinal (v) directions of the shell structure to create a two-dimensional grid of control points (Fig. 6). Unequal spacing is used in the u-direction, where a higher model accuracy is obtained in the curved-crease region. The optimized geometry is defined by $m = 35$ control points in the u-direction (of which 17 to describe the curved crease region) and $n = 56$ equally spaced control points in the v-direction.

Two geometric variants of the structure are chosen for investigation by setting either a small or a large crease radius $r_{t,0}$, resulting in lumped compliance with a distinctive crease (e.g. an origami mechanism) or distributed compliance respectively. Other design variables and material properties used for modeling are denoted in Table 1. Note that not all design parameters are constant throughout the structure, since the flange thickness is allowed to vary in the longitudinal direction, as $t_f = t_f(v)$.

3.2.2. Modeling the transition

The transition is initiated when a transition region forms and an inflection point develops along the spine curve. An effective way to achieve this involved modeling the inverted state by estimating its inverted-state geometry and numerically solving for its closest equilibrium configuration (step 1, Fig. 5). From here, two opposing flange ends are rotated back to their original configuration, while

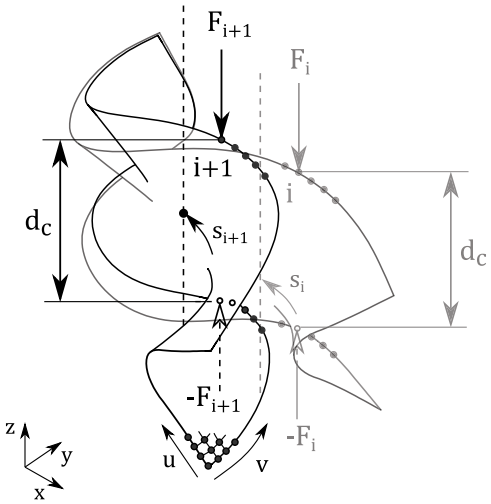

Fig. 6. Material directions u and v generate the two dimensional grid of control points. The transition is modeled by the application of a constraint on the distance d_c between the ith set of two opposing control points on the edges of the shell. F_i and F_{i+1} represent the reaction forces that belong to two consecutive steps. Distance d_c remains constant throughout the transition.

constraining the *opposing* half of the control points on the edge the in vertical(z)-direction (step 2, Fig. 5). Finally, equilibrium is maintained by releasing all but one set of edge constraints that imposes a fixed constraint distance d_c between two symmetrically located control points on opposite edges (step 3, Fig. 5), denoted as the ith set of control points in v-direction (Fig. 6). It is located sufficiently close but behind the inflection point expressed as its location along the spine s.

An effective and reliable method to deform the shell is the application of a constraint distance d_c on subsequent sets of control points along the edges in positive v-direction towards the opposite end. In the case of neutrally stable deformation, the amount of work done should always be zero, irrespective of the chosen method to drive or impose this deformation. In other words, no effort is required to propagate the transition region through the structure. This means that the reaction forces F_i, which result from the applied constraint d_c, should be zero.

In practice, this procedure can be interpreted as 'pinching' the shell structure on its edges and thereby propelling the inflection point forward. The choice for the pinch distance d_c is relevant in order to ensure effective propagation. Because the fully inverted equilibrium state is already known (blue geometry in step 1 of Fig. 5), the distance d_c is chosen to match the distance between the corresponding point-pairs in the inverted equilibrium. This way the external pinching constraint does not cause any additional transversal bending to the inverted structure.

The location of the transition region can be controlled as long as its tendency exists to return to its original position, which is characterized by a positive constraining force F_i. In a general case, this type of structure tends to show this kind of behavior, making it suitable as a stable starting point for an optimization procedure. It must be noted that the point of application of the edge constraint does not coincide with the inflection point, but always lags behind it.

This method of constraining eliminates the need for clamped ends to be applied during the modeling process. This enables the analysis of a free shell and allows for the edge effects to be studied.

The pinching constraint is also used in the experimental validation, see Fig. 7. Utilizing this easy measurable pinching force makes it straightforward to asses the neutrally stable condition.

3.2.3. Optimization procedure

During optimization, the geometry is varied in the search for a unique combination of design parameters that minimizes the objective function, which is defined as the effort required for a transition to occur.

Implementing a thickness variation over the flanges as a variable design parameter allows for fixed coordinates of the control points during variation of the optimization variables. This ensures consistent results from the constraint choice and decreases computing time. The simplest continuous thickness variation can be described by a constant gradient and is chosen as the initial strategy, according to:

$$t_f(v) = a\,\frac{v}{n} + t_{f,0}, \tag{18}$$

where v is a discrete value that denotes the vth set of m control points. This choice requires only two optimization variables:

$$\boldsymbol{x} = [a \quad t_{f,0}]. \tag{19}$$

To promote the existence of a transition region, the optimization window is chosen such that the transition region is located sufficiently far away from the edges, while still including a significant part of the transition. It is achieved by application of the

Table 1
Design parameters used for the optimization procedure.

Parameter	Value	Unit
Geometry		
$r_{t,0}$	$0.01, 0.035$	m
$r_{l,0}$	0.1	m
$\theta_{t,0}$	$\frac{\pi}{2}$	rad
$\theta_{l,0}$	π	rad
w	0.4	m
t_c	$4e^{-4}$	m
t_f	$(a\frac{v}{n} + t_{f,0})$	m
m	35	–
n	56	–
Material		
E	$1.8e^{9}$	$\frac{N}{m^2}$
ν	0.4	–
Optimization		
$\boldsymbol{x}$	$[a \quad t_{f,0}]$	m
$\boldsymbol{x}_{0,r_{t_0}=0.01}$	$[0 \quad 1.6e^{-3}]$	m
$\boldsymbol{x}_{0,r_{t_0}=0.035}$	$[0 \quad 8e^{-4}]$	m
$\boldsymbol{x}_{\min}$	$[0 \quad 3e^{-4}]$	m
x_{tol}	$1e^{-6}$	m
i	$\frac{n}{4} < i < \frac{3n}{4}$	–
d_c	$0.045, 0.060$	m

constraint within boundaries that span the middle half of the structure, given by the interval:

$$\frac{n}{4} < i < \frac{3n}{4}. \tag{20}$$

The objective function in this optimization problem is defined as the sum of all encountered constraining forces, as:

$$f(\boldsymbol{x}) = \sum_{i=\frac{n}{4}}^{\frac{3n}{4}} |F_i|. \tag{21}$$

Note that this value is no measure for the amount of work done since the movement direction of the constraint is perpendicular to its reaction force. Though, it becomes zero when neutral stability is obtained.

Minimizing the value of the objective function is the goal of the optimization procedure. The function *fmincon* from the Matlab® *Optimization toolbox* is employed. The optimization procedure is interrupted when the difference between two consecutive steps of both the objective variables is within the predetermined tolerance $x_{tol} \leq 1e^{-6}$. To ensure a material thickness above a feasible limit from a manufacturing perspective, a lower bound is set on the objective variables, defined by x_{min}. Two optimization runs are performed, i.e. one for each variation of $r_{t,0}$. The initial values for the optimization variables, $\boldsymbol{x}_0$, are denoted in Table 1.

3.2.4. Prototype fabrication

Multi Jet Fusion, an accessible manufacturing method able to deal with the double-curved geometry and variable shell thickness, is used to prototype the two optimized designs. This additive manufacturing technique provides respectable material homogeneity, enables material thickness down to the tenth-of-a-millimeter scale and allows for processing of materials with sufficient elasticity (i.e. high yield strength with respect to E-modulus). The prototypes were constructed out of PA-12 with material properties denoted in Table 2.

Printing orientation determines material homogeneity to a large extent, especially in regions of low thickness. To mitigate the resulting effects, printing orientation is chosen such that the printing layers are oriented parallel to the horizontal construction(xy)-plane, ensuring layer cross-sections with a consistent line-like appearance.

3.3. Experimental validation

3.3.1. Measurement setup

To verify the simulated results, a measurement setup is designed that mimics the modeled conditions (Fig. 7). A measurement frame (1) with two contact points formed by grooved rollers (3,4) serves as the constraint. Rolling is prevented by brake screws and position is maintained by friction between the prototype's edges and the roller surfaces. The distance d_c between the contact points is adjustable and chosen to match the simulated conditions corresponding to each prototype. A $9N$ miniature S-beam load cell (Futek LSB200) is connected to the upper contact point with its measurement axis in line with the direction of the two contact points. Measuring the upward-directed forces along this axis enables elastic reaction forces to be measured while excluding gravitational

Table 2
Details on the 3D-printing process.

Parameter	Value	Unit
Material (PA-12)		
Tensile strength (XY)	$48e^6$	$\frac{N}{m^2}$
Tensile strength (Z)	$48e^6$	$\frac{N}{m^2}$
E (XY)	$1.7e^9$	$\frac{N}{m^2}$
E (Z)	$1.8e^9$	$\frac{N}{m^2}$
Process		
Accuracy	0.3	%
Layer thickness	0.08	mm

Table 3
Optimized results for the optimization variables.

Parameter	Value	Unit
$x_{r_{t_0=0.01}}$	$[1.3411e^{-3} \quad 8.3703e^{-4}]$	m
$x_{r_{t_0=0.035}}$	$[9.5574e^{-4} \quad 3.1856e^{-4}]$	m

forces. The force signal is processed by a signal conditioner (Scaime CPJ2S) before being fed into an acquisition module (NI USB-6008).

After manual initiation of a transition region, the specimen is clamped between the contact points at a number of discrete locations x_c along the edge with intervals of $l_{edge}/10$ and moved manually through the measurement setup. Sliding motion as a result of the parallel component of the reaction force is prevented by friction. The measured force can be directly compared to the constraint force obtained from the model.

4. Results

4.1. Simulation results

This section presents the results of two successful optimization runs that were limited by the convergence criterion of $x_{tol} = 1e^{-6}$ m on the optimization variables. Fig. 8 shows the energetic paths of the two optimized geometries during transition at the beginning and end of the optimization window, denoted with (1) and (2) respectively. Values of the energy are plotted with respect to the locations of the inflection point s (not to be mistaken with the constraint location x_c). The separate energy contributions of the flange and crease sections are indicated by the intermittent lines. Only data points are plotted for configurations that featured an inflection point along the spine, accounting for the abrupt ends. The energy paths for the geometries corresponding to the start of the optimization procedure, see Table 1, are also shown for comparison.

The optimization procedure resulted in an energy variation of less than 4% and 2% of its average within the optimization window for $r_{t_0=0.01}$ and $r_{t_0=0.035}$ respectively. The optimized design variables are presented in Table 3 and the resulting optimized flange thickness gradient t_f along the v-direction is depicted in Fig. 9. The deformation process is shown in Fig. 10, where the volumetric strains are also indicated.

Fig. 11 shows the reaction forces required to maintain equilibrium during transition. Results for $\boldsymbol{x} = \boldsymbol{x}_0$ (i.e. prior to optimization) are represented for comparison by the dashed lines, while the solid lines denote the optimized results. Data points are solely available for configurations where an inflection point on the spine could be localized, resulting in the seemingly abrupt beginning and ending of the plots.

4.2. Experimental results

Neutrally stable behavior was observed on the physical model. In Fig. 13, various stable configurations during the transition from undeformed (1) to an inverted (5) state are depicted.

Fig. 11 shows the measurement results of the reaction forces of both prototypes, which are required to maintain equilibrium throughout the transition process. For comparison, simulated results that are corrected for measured thickness are presented as dashed–dotted lines. The measurement range was limited by the force transducer, causing reaction forces above 20 N not to be measured with the current setup. The markers represent the upper and lower measurement bounds, following from measurements taken in a loading or unloading direction respectively. Zero force measurements (i.e. when contact loss occurred) are denoted with circles. The gray area contains all possible encountered measurements, independent of approach direction and indicates the visco-elastic behavior and hysteresis of the material. Measurements from where 'self propagation' occurred correspond to a negative constraining force and are therefore discarded.

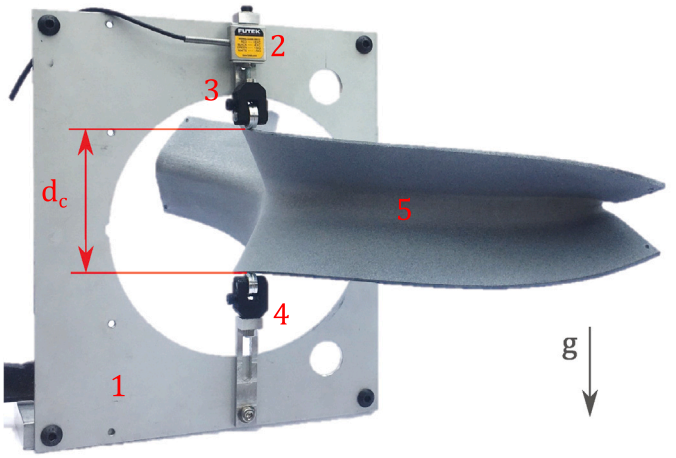

Fig. 7. The experimental setup used to mimic the simulated conditions during transition of the shell. The measurement frame (1) holds the force sensor (2) with primary contact point (3) and the secondary contact point (4). The prototype is clamped between the contact points at a known distance d_c, thereby mimicking the simulations.

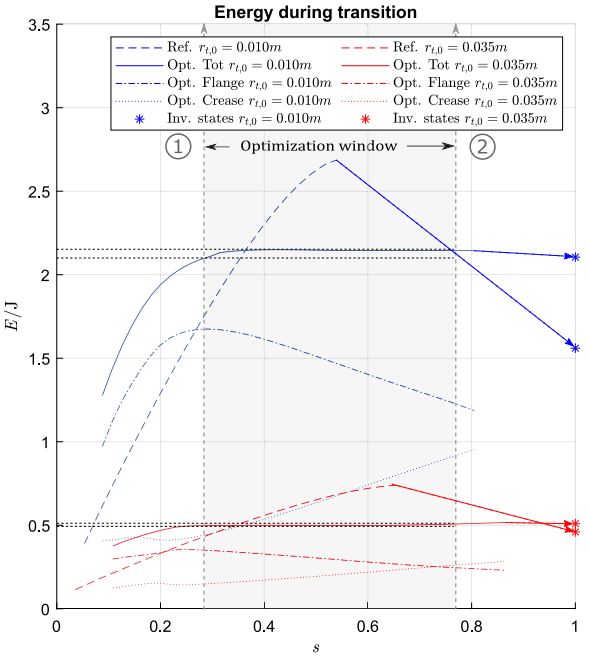

Fig. 8. The resulting energy paths of the shells from two different optimized sets of parameters, with respect to the location of the inflection point s, during propagation of the transition region are depicted. The vertical dashed lines, denoted with (1) and (2) represent the optimization window, i.e. the interval wherein the objective function (Eq. (21)) is defined. The horizontal dashed lines illustrate the energy variation and the markers denote the energy levels of the fully inverted state. The energy paths belonging to the non-optimized shell, i.e. at the start of the optimization, are shown in the dashed lines for comparison. Individual flange- and crease components of the optimized results are plotted by the dashed–dotted and dotted lines respectively.

5. Discussion

5.1. Numerical results

The typical behavior during deformation of a compliant shell is a result of the complex interplay between all parts of its structure. However, an intuitive approach, whereby several sub-functions are attributed to separate parts, turned out to be effective during

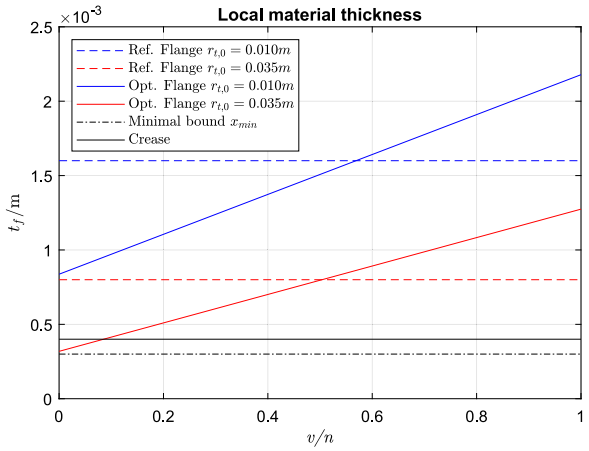

Fig. 9. The optimized local thickness variation $t_f(v)$ of both structures. The crease thickness t_c is constant and equal in both variants. The dash-dotted line represents the optimization minimal bound.

investigation of this particular type of structure. The optimization procedure resulted in behavior similar to the intuitive prediction (Fig. 4), whereby a distinctive loading phase could be identified and the energy increase of the crease region during transition indeed approximates the expected linear course. To compensate, the flanges provide the opposite characteristic, whereby superposition results in a constant energy level, indicating neutral stability. From this perspective, the crease and the flanges can be considered as the load-carrying and compensating elements respectively, similar to the approach taken in most of the previously mentioned existing examples of neutrally stable shell structures (Kok, 2020).

A remarkable outcome is the apparent simplicity of the required optimization parameters, i.e. the linearly varying flange thickness, needed to produce results that approach this unique state of neutral stability very closely. A constant thickness gradient might initially sound like a sensible guess, but close inspection of Eq. (14) reveals a cubic relationship between the material thickness and associated deformation energy. So far, no profound explanation for this phenomenon has been found.

Most of the energy deviations within the optimization window occur around the window's borders, while the majority of the transition features a close-to-constant energy level. This could be explained by edge-effects and the inability of the constant thickness gradient to compensate for it.

Another notable feature of the resulting neutrally stable behavior is the energy level at which it takes place. The objective function is designed to reduce the sum of the constraining forces to zero, creating an energy course with a derivative that approaches zero. No bounds were set to control the energy magnitude: this value is arbitrary. However, in both cases, this energy level matches the energy level of the inverted state closely, suggesting even a smooth transformation between the transition phase and the inverted state. This can indeed be experienced while handling the physical models.

The shell in this investigation is considered to be 'free floating in space', i.e. no constraints are imposed on the structure's boundaries. However, when one would look at this structure as to have a clamped base and a free end-effector, it can be regarded as a beam element that exhibits neutral stability in its bending degree of freedom. This lays the foundation for compliant building blocks with a beam-like appearance and -kinematic behavior that are neutrally stable.

5.2. Experimental results

Measurements on the dimensions revealed a disparity between the digital models and the physical prototypes. Because of the small thicknesses, deviations easily cause large relative differences. In combination with the cubic relation between material thickness and associated elastic energy, behavior is expected to be most sensitive to this metric. Measurements taken along the circumference of both prototypes show that differences as high as 50% occurred (Fig. 12).

The hysteresis loop observed in Fig. 11 is caused by internal friction of the material. Energy dissipation within the material enables no reaction force to be measured if the hysteresis band crosses the zero-force line. Hysteresis causes a continuous state of equilibrium along the range of motion, which gives the false appearance of a perfect neutral stability. It is therefore difficult to asses real elastic neutral stability in the presence of visco-elastic resistance.

Hysteresis loss is more notably present in the design that requires higher reaction forces, corresponding to $r_{t,0} = 0.01$ m. Apart from a larger average thickness, this shell features higher strains during transition (Fig. 10) as a possible cause for higher energetic losses. Finally, gravity was not taken into account in the numerical analysis and, although the experimental setup avoids measuring weight, the presence of a gravitational field does affect the structure's deformed geometry. However, this effect is assumed to be negligible compared to the effects caused by the elastic forces.

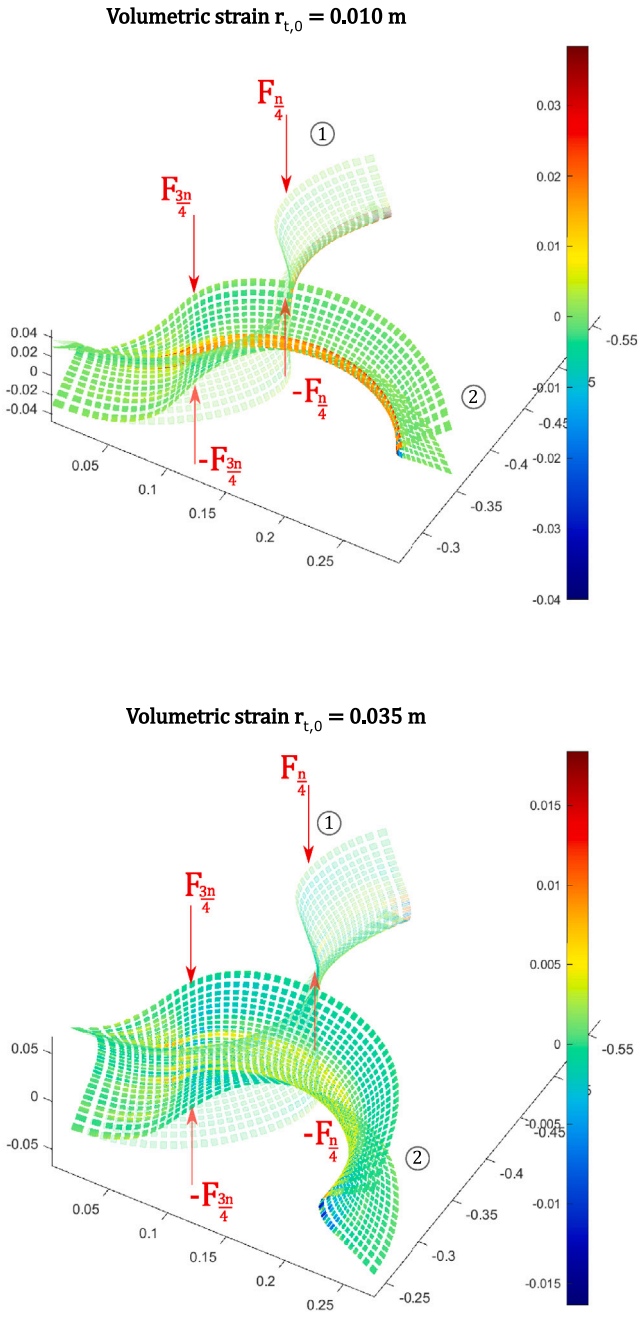

Fig. 10. The deformation process during transition and associated volumetric strains, belonging to configurations at the beginning (opaque) and end (translucent) of the optimization window, denoted with (1) and (2) in Fig. 8 respectively.

5.3. Future work

Development of the optimization process towards other, conventional, manufacturing methods as well is desired to increase its applicability. Prior research (Kok et al., 2021) has shown promising results in the optimization of geometric properties, e.g. local flange width and local longitudinal curvature, to influence the energetic path during transition. This allows for a structure with a uniform thickness that is not solely bound to additive manufacturing processes, but allows for, e.g., sheet forming techniques as well. Furthermore, the lack of stiffness in lateral directions makes this structure unsuitable for applications where structural integrity is required.

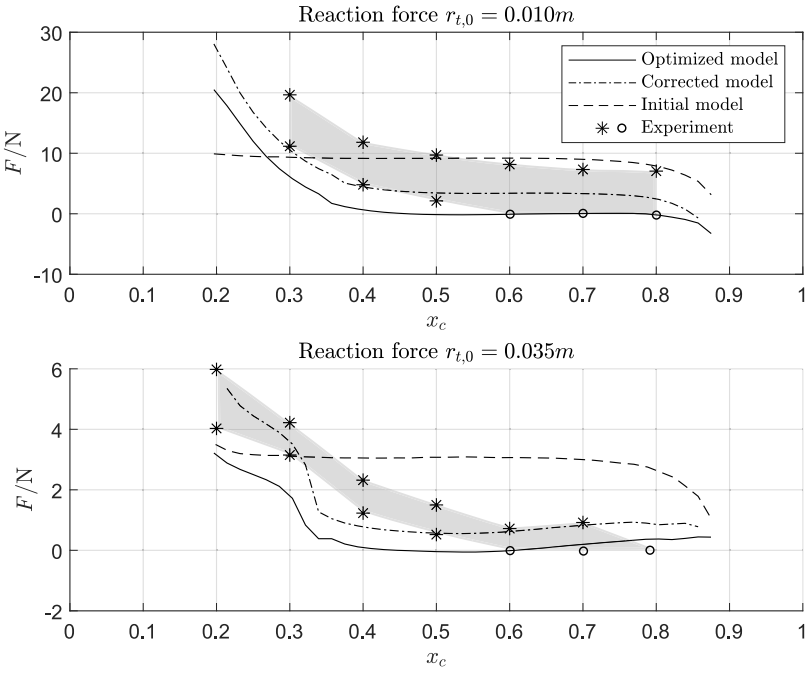

Fig. 11. Experimental results of the reaction forces required to maintain equilibrium are depicted by their upper and lower boundaries (markers), corresponding to the loading and unloading directions respectively. Optimized modeled results are presented by the solid lines and the modeled results, compensated for the prototype thickness, are depicted as dashed-dotted lines. The reaction forces that belong to the starting parameters of the optimization procedure x_0 are represented by the dashed lines.

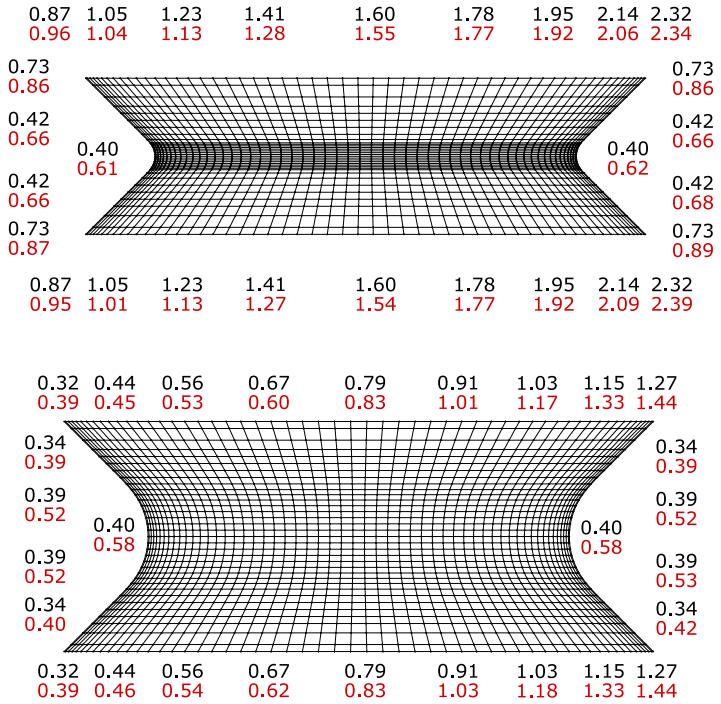

Fig. 12. Measurements on the local thickness of the two prototypes (red) is compared to the local thickness of the optimized modeled geometry (black). Measurements are only performed on the accessible perimeter of the shells.

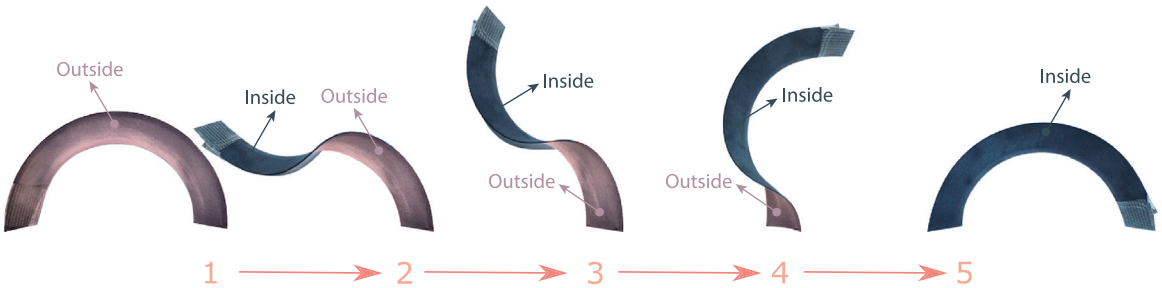

Fig. 13. Physical model in several stable configurations during transition from the undeformed (1) to the inverted (5) state. A continuous equilibrium was observed in this physical model (see supplementary video).

6. Conclusion

In this investigation, the transition between the undeformed and inverted equilibrium configurations of a double-curved shell structure is analyzed. The approach, that involved functional separation of the parts within this distributed compliant shell, turned out to be useful for the creation of a neutrally stable deformation mode. Optimization of the design parameters resulted in a constant energy level within a significant portion of the transition. Therefore, we present a new class of neutrally stable shell structure that, in contrast to examples in the literature, does not rely on pre-stress obtained during the manufacturing process or boundary conditions to be imposed. Instead, it features neutral stability as part of a continuous deformation process, allowing a stress-free configuration to exist.

Successful optimization runs, based on a variable material thickness, resulted in shell structures with a significant near-constant-energy region as part of their transition. Ultimately, the physical realization of additively manufactured prototypes validates the modeled results by featuring infinitely many equilibrium configurations along the deformation path. Remarkably, a relatively simple constant thickness gradient of the flange sections over the length of the structure is sufficient for this unique behavior to occur. An explanation thereof has not yet been given.

The proposed shell structure can be considered as a beam element with a neutrally stable bending degree of freedom, laying the foundation for neutrally stable building blocks with a beam-like appearance and kinematic behavior. However, despite the progress made, the variable material thickness throughout the structure limits the manufacturing method to additive manufacturing techniques. Other tactics to tune the behavior that allow for a uniform material thickness (Kok et al., 2021) could be investigated to facilitate manufacturing and applicability.

CRediT authorship contribution statement

Sjaak Kok: Conceptualization, Methodology, Software, Validation, Writing – original draft, Visualization. **Ali Amoozandeh Nobaveh:** Writing – review & editing, Visualization, Supervision. **Giuseppe Radaelli:** Conceptualization, Methodology, Software, Writing – review & editing, Supervision.

Declaration of competing interest

The authors declare that they have no known competing financial interests or personal relationships that could have appeared to influence the work reported in this paper.

Data availability

No data was used for the research described in the article.

Acknowledgments

This work was supported by the Dutch Research Council (NWO), The Netherlands [P16-05 Shell-Skeletons].

Appendix A. Supplementary data

Supplementary material related to this article can be found online at https://doi.org/10.1016/j.jmps.2022.105133.

References

Alkisaei, H., 2016. Statically balanced compliant walls. URL http://repository.tudelft.nl/islandora/object/uuid%3A4d8e476f-b02f-4abe-b0e4-47c97f958fbd?collection=education%5Cnhttp://repository.tudelft.nl/islandora/object/uuid%3A4d8e476f-b02f-4abe-b0e4-47c97f958fbd/datastream/OBJ/view.

Amoozandeh Nobaveh, A., Radaelli, G., Herder, J.L., 2020. Asymmetric spatial beams with symmetric kinetostatic behaviour. In: Symposium on Robot Design, Dynamics and Control. Springer, pp. 247–254. http://dx.doi.org/10.1007/978-3-030-58380-4_30.

Amoozandeh Nobaveh, A., Radaelli, G., Herder, J.L., 2022. Symmetric kinetostatic behavior from asymmetric spatially curved beams. J. Mech. Robot. 1–10. http://dx.doi.org/10.1115/1.4055419, arXiv:https://asmedigitalcollection.asme.org/mechanismsrobotics/article-pdf/doi/10.1115/1.4055419/6913333/jmr-21-1645.pdf.

Audoly, B., Boudaoud, A., 2002. 'Ruban à godets': An elastic model for ripples in plant leaves. Compt. R. - Mec. 330 (12), 831–836. http://dx.doi.org/10.1016/S1631-0721(02)01545-0.

Calladine, C., 1989. Theory of Shell Structures. Cambridge University Press, Cambridge, p. 763.

Daynes, S., Lachenal, X., Weaver, P.M., 2015. Concept for morphing airfoil with zero torsional stiffness. Thin-Walled Struct. 94, 129–134. http://dx.doi.org/10.1016/j.tws.2015.04.017.

Daynes, S., Weaver, P.M., 2013. Stiffness tailoring using prestress in adaptive composite structures. Compos. Struct. 106, 282–287. http://dx.doi.org/10.1016/j.compstruct.2013.05.059.

Doornenbal, B., 2018. Zero Stiffness Composite Shells: Using Thermal Prestress (Msc thesis). (September), Delft University of Technology, URL http://repository.tudelft.nl/.

Gallego, J.A., 2013. Statically balanced compliant mechanisms: theory and synthesis. pp. 1–219. http://dx.doi.org/10.4233/uuid:081e3d0e-173b-4a36-b8d6-c29c70eb7ae3, URL http://repository.tudelft.nl/view/ir/uuid:081e3d0e-173b-4a36-b8d6-c29c70eb7ae3/.

Galletly, D.A., Guest, S.D., 2004. Bistable composite slit tubes. II. A shell model. Int. J. Solids Struct. 41 (16–17), 4503–4516. http://dx.doi.org/10.1016/j.ijsolstr.2004.02.037.

Giomi, L., Mahadevan, L., 2012. Multi-stability of free spontaneously curved anisotropic strips. Proc. R. Soc. A: Math., Phys. Eng. Sci. 468, 511–530. http://dx.doi.org/10.1098/RSPA.2011.0247, URL https://royalsocietypublishing.org/doi/10.1098/rspa.2011.0247.

Goriely, A., 2017. The Mathematics and Mechanics of Biological Growth. Springer Nature, New York.

Guest, S., 2011. Zero stiffness elastic shell structures. Mech. Mater. Struct. 6 (7).

Herder, J., Van Den Berg, F., 2000. Statically balanced compliant mechanisms, an example and prospects. In: Proceedings of the 26th ASME DETC Biennial, Mechanisms and Robotics Conference.

Howell, L.L., Magleby, S.P., Olsen, B.M., 2013. Handbook of Compliant Mechanisms. John Wiley & Sons, New York.

Hughes, T.J., Cottrell, J.A., Bazilevs, Y., 2005. Isogeometric analysis: CAD, finite elements, NURBS, exact geometry and mesh refinement. Comput. Methods Appl. Mech. Engrg. 194 (39–41), 4135–4195. http://dx.doi.org/10.1016/j.cma.2004.10.008.

Knott, G.P., Viquerat, A., 2016. Modeling the Bistability of Laminated Composite Toroidal Slit Tubes (June) http://dx.doi.org/10.2514/6.2016-1499.

Knott, G., Viquerat, A., 2018. Curved bistable composite slit tubes with positive Gaussian curvature. AIAA J. 56 (4), 1679–1688. http://dx.doi.org/10.2514/1.J056411.

Knott, G., Viquerat, A., 2019. Helical bistable composite slit tubes. Compos. Struct. 207 (May 2018), 711–726. http://dx.doi.org/10.1016/j.compstruct.2018.09.045.

Kok, S., 2020. Towards Neutrally Stable Compliant Shells (Msc thesis). Delft University of Technology, http://repository.tudelft.nl/.http://resolver.tudelft.nl/uuid:e50b249c-63ad-4f85-8fdc-d90488965f07.

Kok, S., Radaelli, G., Amoozandeh Nobaveh, A., Herder, J., 2021. Neutrally stable transition of a multi-stable curved crease compliant shell structure. Extreme Mech. Lett. 49 (November 2021), http://dx.doi.org/10.1016/j.eml.2021.101469.

Lachenal, X., Daynes, S., Weaver, P.M., 2013. A zero torsional stiffness twist morphing blade as a wind turbine load alleviation device. Smart Mater. Struct. 22 (6), http://dx.doi.org/10.1088/0964-1726/22/6/065016.

Lachenal, X., Weaver, P.M., Daynes, S., 2012. Multi-stable composite twisting structure for morphing applications. Proc. R. Soc. A: Math., Phys. Eng. Sci. 468 (2141), 1230–1251. http://dx.doi.org/10.1098/rspa.2011.0631.

Lessinnes, T., Moulton, D.E., Goriely, A., 2017. Morphoelastic rods Part II: Growing birods. J. Mech. Phys. Solids 100 (September 2014), 147–196. http://dx.doi.org/10.1016/j.jmps.2015.07.008.

Murphey, T.W., Pellegrino, S., 2004. A novel actuated composite tape-spring for deployable structures. In: Collection of Technical Papers - AIAA/ASME/ASCE/AHS/ASC Structures, Structural Dynamics and Materials Conference, Vol. 1. pp. 260–270. http://dx.doi.org/10.2514/6.2004-1528.

Radaelli, G., Herder, J.L., 2015. A monolithic compliant large-range gravity balancer. In: 2015 IFToMM World Congress Proceedings, IFToMM 2015. http://dx.doi.org/10.6567/IFToMM.14TH.WC.OS20.018.

Radaelli, G., Herder, J.L., 2017. Gravity balanced compliant shell mechanisms. Int. J. Solids Struct. 118–119, 1339–1351. http://dx.doi.org/10.1016/j.ijsolstr.2017.04.021.

Schultz, M.R., Hulse, M.J., Keller, P.N., Turse, D., 2008. Neutrally stable behavior in fiber-reinforced composite tape springs. Composites A 39 (6), 1012–1017. http://dx.doi.org/10.1016/j.compositesa.2008.03.004.

Stacey, J.P., O'Donnell, M.P., Schenk, M., 2019. Thermal prestress in composite compliant shell mechanisms. J. Mech. Robot. 11 (2), 1–10. http://dx.doi.org/10.1115/1.4042476.

Vehar, C., Kota, S., Dennis, R., 2004. Closed-loop tape springs as fully compliant mechanisms -preliminary investigations. In: Proceedings of the ASME Design Engineering Technical Conference, Vol. 2 B. pp. 1023–1032. http://dx.doi.org/10.1115/detc2004-57403.